CrossMark

ORIGINAL PAPER

Highly efficient visible-light photocatalyst based on cellulose derived carbon nanofiber/BiOBr composites

Aobo Geng · Liang Meng · Jingquan Han · Qiang Zhong · Meirun Li · Shuguang Han · Changtong Mei · Lijie Xu · Lin Tan · Lu Gan

Abstract There is an urgent need to explore alternatives to replace traditional carbonaceous materials because of dwindling oil reserves and increasing atmospheric carbon dioxide. In the present study, the cellulose derived carbon nanofibers (CCNF) were prepared and used to hybridize with bismuth oxybromide to prepare novel photocatalyst composites (CCNF/BiOBr). The structural properties of the prepared composites were then characterized. Afterwards, the photocatalytic performance of the CCNF/BiOBr composites was investigated through degrading rhodamine B (RhB) under continuous visible light irradiation. The results indicated that the pyrolysis process could convert the cellulose to carbon nanofiber with high graphitization degree. The photocatalytic performance of the CCNF/BiOBr composite was better than that of the pure BiOBr, which was ascribed to the introduction of the CCNF into the composite system. The present work provides a promising way to design new photocatalyst composites with desirable carbon alternatives from biomass materials for effective treatment of organic contaminants in water media.

A. Geng · J. Han · Q. Zhong · M. Li · S. Han ·
C. Mei · L. Gan (✉)
College of Materials Science and Engineering, Nanjing Forestry University, Nanjing 210037, Jiangsu, People's Republic of China
e-mail: ganlu@njfu.edu.cn

L. Meng · L. Xu
College of Biology and the Environment, Nanjing Forestry University, Nanjing 210037, Jiangsu, People's Republic of China

L. Tan
College of Light Industry, Textile and Food Engineering, Sichuan University, Chengdu 610065, China

Graphical Abstract
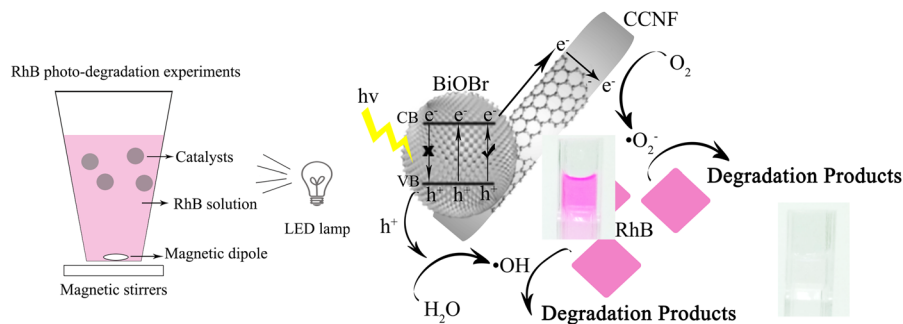
Keywords Cellulose · Carbon nanofiber · Pyrolysis · Visible-light photocatalyst · Pollutant degradation

Introduction

In the past two decades, photocatalytic technology has received considerable attention for the treatment of environmental contaminants, particularly in water purification (Chen et al. 2018; Gan et al. 2016a). Among multifarious photocatalysts, the Bi-based catalysts, especially bismuth oxyhalide (BiOX, X = F, Cl, Br, I), have demonstrated greater potential and attracted more interest because of their outstanding properties, such as low cost, lower toxicity and the possibility of reuse (Choi et al. 2015; Liu et al. 2018). More importantly, the unique ternary molecular structure, a suitable band gap and excellent fluorescence properties enable the BiOX family to have higher photocatalytic capability for the degradation of organic pollutants in water under ultraviolet (UV) or visible light irradiation (Ao et al. 2014). Among several BiOX compounds, BiOBr shows an appropriate band gap of 2.75 eV, which makes it superiorly responsive at visible light irradiation, and therefore BiOBr has been extensively investigated recently in photocatalytic degradation of various organic compounds (Jiang et al. 2016; Yuan et al. 2016). However, since the BiOBr has a positive conduction band (CB) potential (0.22 eV vs NHE) and a more negative Bi^{4+}/Bi^{3+} standard redox potential (1.59 eV), it shows a rapid recombination of the photo-generated electrons and holes, which restricts its efficiency in photocatalytic processes (Ai et al. 2009).

Meanwhile, a number of studies have demonstrated that the doping of the carbonaceous materials, such as graphene, carbon nanofiber (CNF) and carbon nanotubes (CNTs), with the photocatalyst can significantly improve the photocatalytic efficiency of a pristine photocatalyst (Gan et al. 2016b; Xu et al. 2017). These carbonaceous materials have conjugated graphitic structures within their skeleton, which can effectively reduce the band gap and decrease the electron–hole recombination chance of the photocatalysts (Hu et al. 2014; Huang et al. 2017). However, most carbonaceous materials are derived from dwindling oil resources. Therefore, other desirable carbon alternatives are urgently need to replace traditional carbonaceous materials. As a representative, cellulose from natural biomass has the advantages of being abundant, eco-friendly, inexpensive, and renewable (Wu et al. 2015a, b). Recent studies have shown that through an electrospinning and a subsequent pyrolysis treatment under oxygen-limited conditions, the cellulose could be turned to carbon-enriched nanofiber materials (CCNF) (Cai et al. 2016; Jazaeri et al. 2011). Compared with biomass derived bulk carbon, nanosized biochar could enhance the photocatalytic performance of a photocatalyst more significantly due to higher specific areas (Carpenter et al. 2015). Moreover, the electrospinning technique could provide cellulose nanofibers with regular shapes and uniform fiber diameters, when compared with those obtained from traditional acidified treatment (Liu and Hsieh 2002). Thus, hopefully this biochar CCNF can be a promising alternative to the petroleum derived carbon nanomaterials. It can be also predicted that the replacement of petroleum derived carbon resources to biochar nanomaterials not only saves the oil resources significantly, but also enriches the

application potentials of biomass materials in the environmental field. While until recently, studies concerned with the improvement of the photocatalytic capabilities of photocatalysts by CCNF are still very limited.

Therefore, based on the above facts, composite photocatalysts hybridizing BiOBr and the cellulose based carbon-enriched nanofibers (CCNF/BiOBr) were prepared in the present study. The morphology and structure of the synthesized photocatalysts were characterized afterwards. The photocatalytic performance of the CCNF/BiOBr under visible light irradiation was then studied using rhodamine B (RhB) dye as the target pollutant and the LED lamp as the visible light source. Through examining the influence of catalyst dosage, CCNF content, initial RhB concentration and solution pH value, the photocatalytic properties of the prepared photocatalysts was investigated in detail.

Experimental section

Materials

The cellulose acetate (CA) (Acetyl 39.8 wt%, hydroxyl 3.5 wt%) was purchased from Aladdin Industrial Co., Ltd. (Shanghai, China). Bismuth(III) nitrate pentahydrate [$Bi(NO_3)_3 \cdot 5H_2O$] was purchased from Sinopharm Chemical Reagent Co., Ltd. (Shanghai, China). Sodium bromide (NaBr) was purchased from Yonghua Chemical Technology Co., Ltd. (Shanghai, China). Ethylene glycol (EG) was purchased from Shanghai No.4 Reagent & H.V. Chemical Co., Ltd. (Shanghai, China). RhodamineB (RhB) was purchased from Shanghai Macklin Biochemical Co., Ltd. (Shanghai, China). Other chemicals used in this study were analytical grade and used as received without further treatment.

Preparation of CCNF/BiOBr composites

The cellulose nanofibers were prepared by electrospinning approach according to the previous study (Tan et al. 2017). CCNF was obtained by pyrolysis treatment under nitrogen atmosphere. The obtained cellulose nanofibers were transferred into a ceramic crucible and heated to 400 °C at the rate of 5 °C/min, maintained at 400 °C for 1 h, and then heat up to

800 °C at the rate of 5 °C/min and kept at 800 °C for another 3 h. After the temperature was cooled to room temperature naturally, the CCNF was obtained.

The synthesis of CCNF/BiOBr composites uses a hydrothermal process described as follows. Typically, certain amount of CCNF was dispersed in 100 mL of EG, magnetically stirred for 2 h and sonicated for another 2 h. 2.92 g of $Bi(NO_3)_3 \cdot 5H_2O$ was then dissolved in the obtained homogenous dispersion and stirred for another 20 min. After 2.06 g of NaBr was added and dissolved, the mixture was put into a Teflon-lined autoclave and kept at 160 °C for 24 h. The precipitate was washed with distilled water for 3 times. After being air-dried at 60 °C for 24 h and then dried under vacuum at 80 °C for another 24 h, the as-prepared CCNF/BiOBr composites with CCNF contents of 0.5, 1.0, 2.0, and 4.0 wt% were finally obtained, and named as 0.5CCNF/BiOBr, 1.0CCNF/BiOBr, 2.0CCNF/BiOBr and 4.0CCNF/BiOBr, respectively. For comparison, pure BiOBr was also prepared according to similar procedures. The preparation procedures of the CCNF/BiOBr composites were schematic illustrated in Fig. 1.

Characterizations

The morphology of the prepared composites was observed by scanning electron microscopy (SEM) using the FEI Quanta 200. Fourier transform infrared (FT-IR) spectra were recorded by a Bruker Vertex80v at wavenumbers ranging from 4000 to 450 cm^{-1} with a resolution of 4 cm^{-1} and 16 scans. The X-ray diffraction (XRD) was conducted using a Rigaku Ultima IV XRD instrument with the Cu-Kα as the radiation source 1.54 Å). Raman spectra were performed using a Thermo DXR532 Raman spectrometer, which was equipped with an Ar laser (532 nm, 180 mW) as the excitation light source, and a microscope. The diffuse reflectance spectra (DRS) were conducted by a Perkin Elmer Lambda 950 UV/Vis/NIR spectrophotometer. The photoluminescence (PL) spectra of the microspheres were conducted by Perkin-Elmer LS55 spectrofluorometer with a Xe lamp as the excitation source. The excitation wavelength was selected as 350 nm.
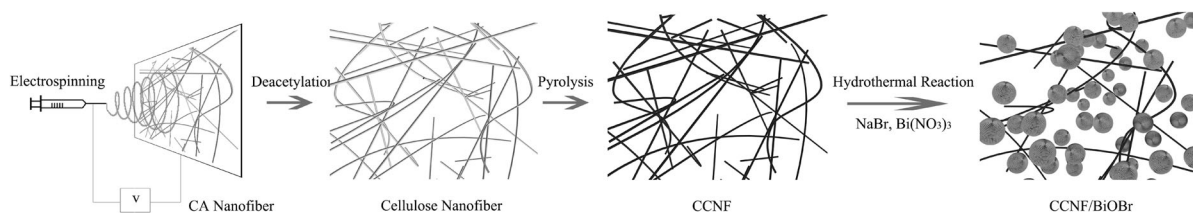
Fig. 1 Schematic illustration of the preparation procedures of the CCNF/BiOBr

Photocatalytic activities measurement
of the prepared CCNF/BiOBr composites

A LED lamp with 200 W output power was used as the visible-light source for photocatalytic experiments and a quartz beaker was used as the reaction vessel at ambient temperature. The emission spectrum of the LED lamp was recorded by a Tianjin Gangdong WGD-8/8A multi-grating spectrometer with the result shown in Fig. S1. In a typical dye degradation experiment, certain amount of RhB stock solution was withdrawn and diluted to 100 mL to prepare the reaction solution with different initial concentrations of 10, 20, 30, 40 and 50 mg/L, respectively.

After certain amount of catalyst was added into the dye solution, the mixture was first magnetically stirred in the dark for 30 min to achieve an adsorption–desorption equilibrium, and then placed in front of the LED lamp with a fixed distance of 15 cm. The photocatalytic reaction unit was shown in Fig. S2. During the photocatalytic process, approximate 3.0 mL of the mixture was withdrawn at predetermined intervals (0, 5, 10, 15, 30, 60, 90 min), which was filtered immediately to separate solids and further quantified using the UV–Vis spectrometer (Shanghai Jingke722 N UV–Vis spectrometer) at 520 nm.

Results and discussion

Figure 2 displays the SEM images of the CA nanofibers, cellulose nanofibers, CCNF, pure BiOBr, and CCNF/BiOBr composites. As could be seen from Fig. 2a–c, the diameters of electrospun CA nanofibers and cellulose nanofibers were uniform. Meanwhile, the CCNF became curly after pyrolysis, but still maintained the initial shape of nanofibers. It could be seen from Fig. 2d that the pure BiOBr had a microsphered morphology with well-dispersed and homogeneous particle size distributions. When the CCNF

was incorporated into the composites, the BiOBr microspheres could also be well dispersed and attached to CCNF, without destroying the inherent structure of the BiOBr. The overall SEM results suggested the formation of uniformly structured CCNF/BiOBr composites.

The FT-IR spectra of CA nanofibers, cellulose nanofibers, CCNF, pure BiOBr, and CCNF/BiOBr composites were shown in Fig. 3. As was observed in Fig. 3a, the CA nanofibers had characteristic peaks at ~ 3450, 1750, 1635 and 1040 cm^{-1}, which were corresponding to the stretching vibration of the –OH groups, stretching vibration of the C=O groups, stretching vibration of the cyclic C–O–C, respectively (Azzaoui et al. 2014). After deacetylation, the peak at ~ 3450 cm^{-1} became broader and shifted to a lower wavenumber at ~ 3325 cm^{-1}. Moreover, the peak at 1750 cm^{-1}, which was ascribed to the stretching vibration of the C=O groups disappeared, indicating that all the C=O ester groups have been turned to the –OH groups. The FT-IR results demonstrated that the CA nanofibers were converted to cellulose nanofibers after the deacetylation reaction.

From the FT-IR spectrum of the CCNF, it could be seen that the intensity of the stretching vibration peak of –OH groups obviously became weaker. It was noted that the peak at 2920 cm^{-1} which was assigned to the C–H stretching vibration also disappeared. Instead, new peaks at 1580 and 1400 cm^{-1} which were ascribed to the stretching vibration of aromatic benzene ring appeared. These results demonstrated that the cellulose skeleton was converted to the graphitic structure of amorphous carbon nanofibers during the pyrolysis process.

Figure 3b shows the comparison of FT-IR spectra of both the obtained BiOBr and CCNF/BiOBr samples. Due to the relatively low amounts of the incorporated CCNF in the photocatalysts, the peaks of the CCNF could not be distinctly observed in the CCNF/BiOBr composites. It could be also seen that all

Fig. 2 SEM images of
a CA nanofibers, b cellulose
nanofibers, c CCNF, d pure
BiOBr, e 0.5CCNF/BiOBr,
f 1.0CCNF/BiOBr,
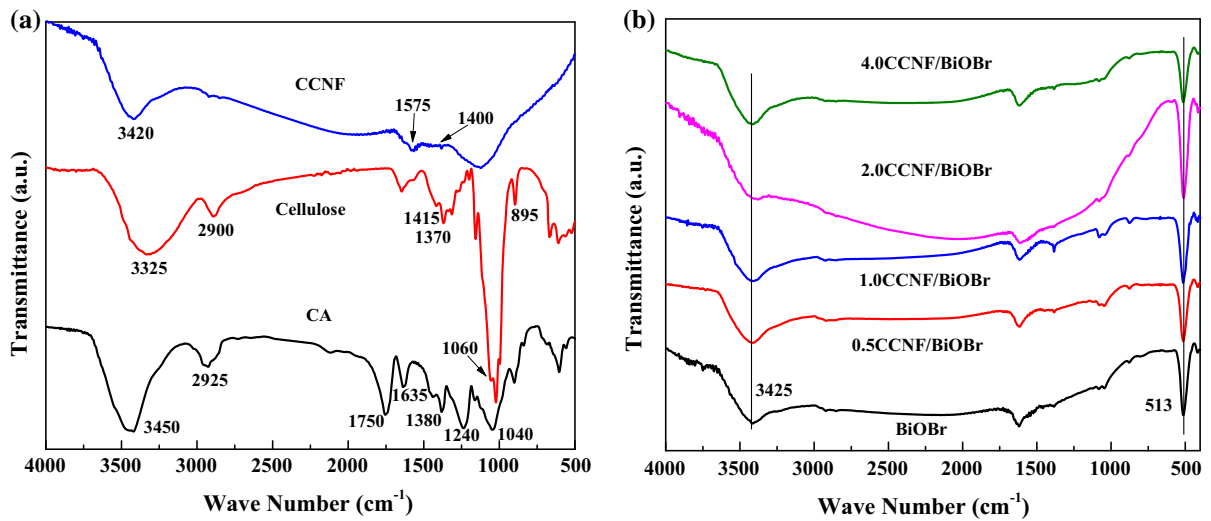g 2.0CCNF/BiOBr and h 4.0
CCNF/BiOBr
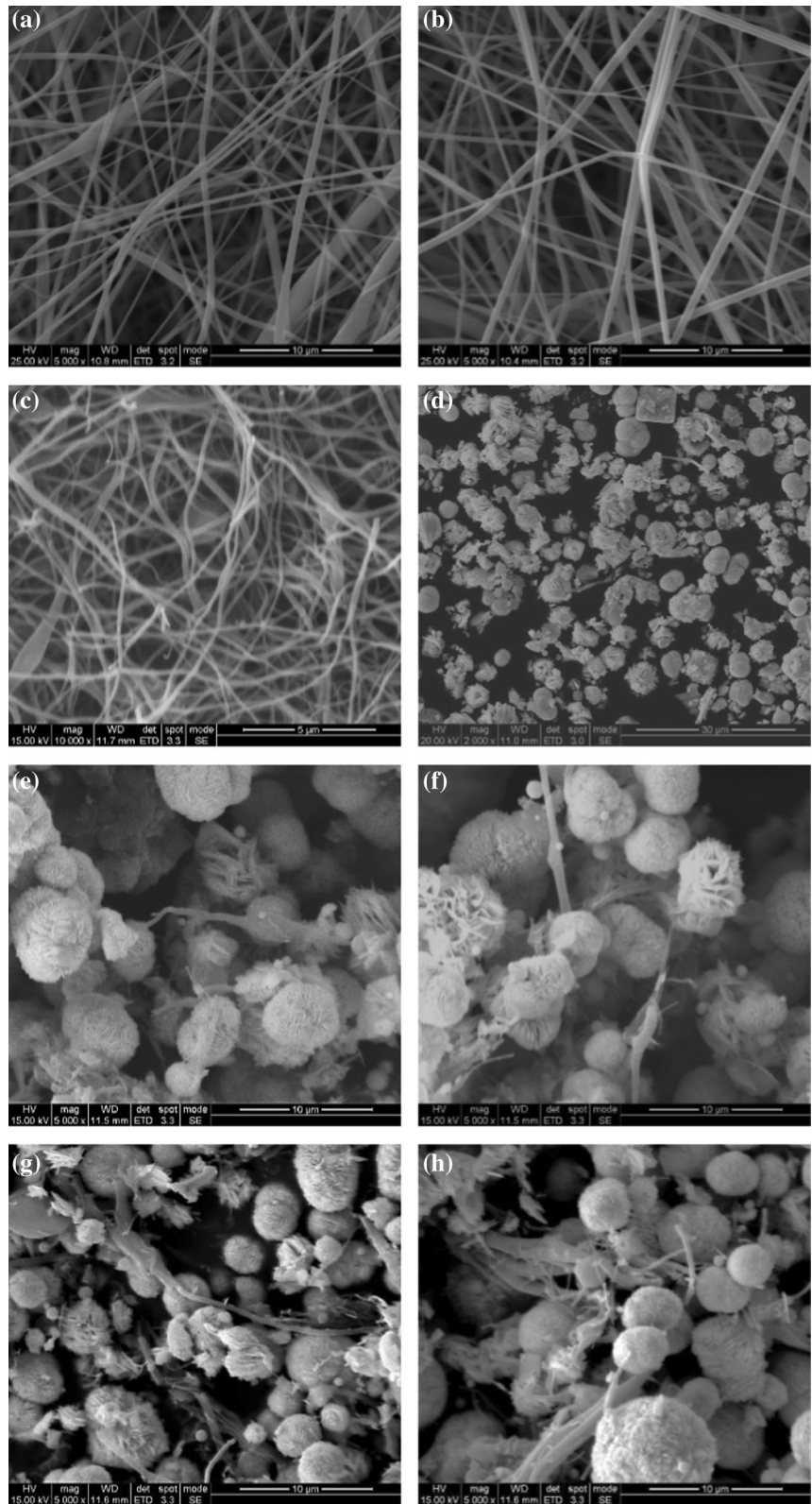
Fig. 3 FT-IR spectra of **a** CA nanofibers, cellulose nanofibers and CCNF, **b** pure BiOBr, 0.5CCNF/BiOBr, 1.0CCNF/BiOBr, 2.0CCNF/BiOBr and 4.0 CCNF/BiOBr

BiOBr based composites had similar spectra to that of the pure BiOBr, indicating that the incorporation of the CCNF into the system did not affect the crystalline structure of BiOBr in hydrothermal synthesis process, and the BiOBr could in-situ formed on the nanofibers, which was in accordance with the SEM results.

The XRD patterns of the CA nanofibers, cellulose nanofibers, CCNF, pure BiOBr, and CCNF/BiOBr were then recorded with the results shown in Fig. 4a. It could be seen that the CA nanofibers and cellulose nanofibers had characteristic peaks at ∼12°, 20° and 22°, which were corresponded to the amorphous

Cellulose II structure (de Moraes et al. 2015). After pyrolysis, these peaks disappeared and two new peaks at ∼26° ∼44° appeared (inset figure), which were corresponded to the (002) and (100) planes of the graphite structure respectively (Pi et al. 2015). This indicated that by suitable pyrolyzation treatment, the crystalline cellulose has been converted to amorphous carbon, which endowed the obtained CCNF with graphitic structure within its skeleton. In addition, it was also clearly observed from Fig. 4a that all the diffraction peaks of pure BiOBr was in good agreement with the tetragonal phase of BiOBr (JCPDS
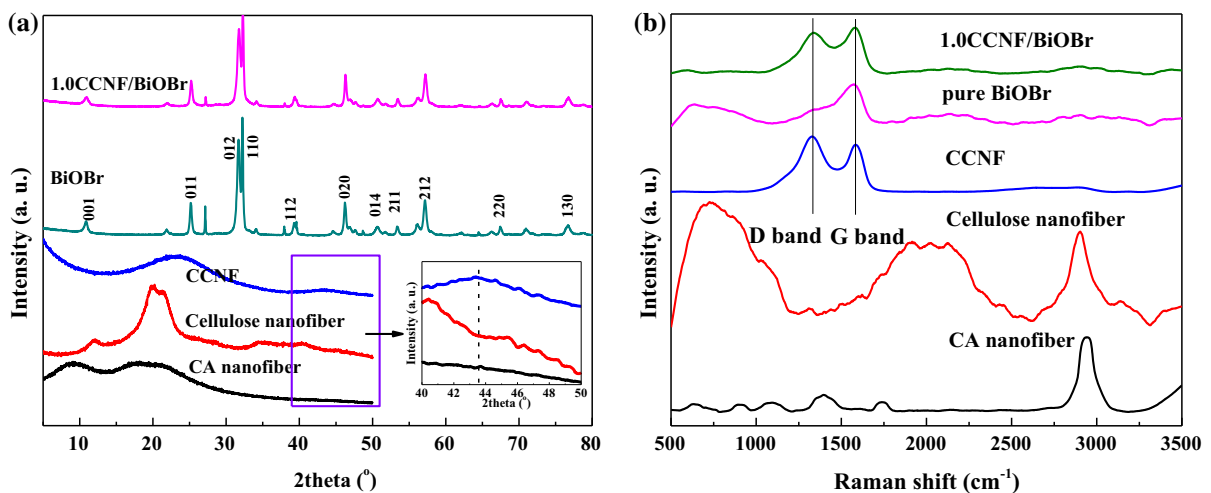

Fig. 4 a XRD patterns and **b** Raman spectra of CA nanofibers, cellulose nanofibers, CCNF, pure BiOBr and 1.0CCNF/BiOBr

73-2061). Compared with pure BiOBr, the CCNF/BiOBr composites had similar diffraction patterns but with decreased peak intensity, which meant that the addition of CCNF slightly decreased the inherent crystalline structure of the BiOBr.

The existence of the graphitic structure in CCNF and CCNF incorporated photocatalysts could be further investigated by Raman spectroscopy as was shown in Fig. 4b. It is generally known that the carbonaceous materials had two specific Raman peaks at ~ 1350 and ~ 1600 cm^{-1} (D band and G band), which were the direct features of the graphitic structure (Gan et al. 2015). It could be seen from Fig. 4b that these two bands were not observable from CA and cellulose nanofibers spectra, indicating the absence of the graphitic structure in these two materials. On the other hand, the CCNF and CCNF/BiOBr composites all demonstrated very obvious and strong D band and G band peaks after pyrolysis, which indicated the formation of the graphitic structure in the carbonaceous CCNF. It was also known that the intensity ratio of D band and G band I$_D$/I$_G$) is often used to speculate the degree of the structure defect. It could be also seen from Fig. S3 that all the I$_D$/I$_G$ values of the CCNF/BiOBr composites were lower than that of the CCNF, indicating that a further hydrothermal process decreased the structure defects of the CCNF and provided higher degree of graphitic structure to the CCNF (Ramirez et al. 2017).

The PL spectra was used to analyze the electron–hole recombination rates of the photocatalysts with the results shown in Fig. 5a. It was noted that pure BiOBr showed a strong emission peaks at 505 nm, which was caused by the recombination of photo-excited electrons at the conduction band (CB) with holes at the valence band (VB). When the CCNF was incorporated, it was obvious that the PL intensity had a gradual decrement trend from the pure BiOBr to 4.0CCNF/BiOBr, and the PL intensity attenuated more significantly with the increase of CCNF content in the composite of CCNF/BiOBr. These phenomena showed that the degree of electron–hole pair recombination of the catalysts was effectively inhibited by the graphitized CCNF with high electron mobility. Therefore, the incorporation of the CCNF could lead to a prolonged lifetime of the photogenerated holes, which could largely enhance the photocatalytic capability of the BiOBr.

The light absorbing performance of pure BiOBr and CCNF/BiOBr composites were examined by DRS with the results shown in Fig. 5b. It could be seen that each photocatalyst had its respective absorption to the light from UV region to the visible region. Particularly, pure BiOBr mainly demonstrated UV range absorption and the absorption edge was around 420 nm. The involvement of various CCNF contents of the CCNF/BiOBr samples led to significant enhancement of the light absorption capability. One could observe that the absorption intensities of the CCNF/BiOBr composites in the visible range were significantly increased with obvious red shift of the absorption edge, in which the absorption edge of the as-prepared composites was extended from 420 to 730 nm with the increase of CCNF content to 4 wt%
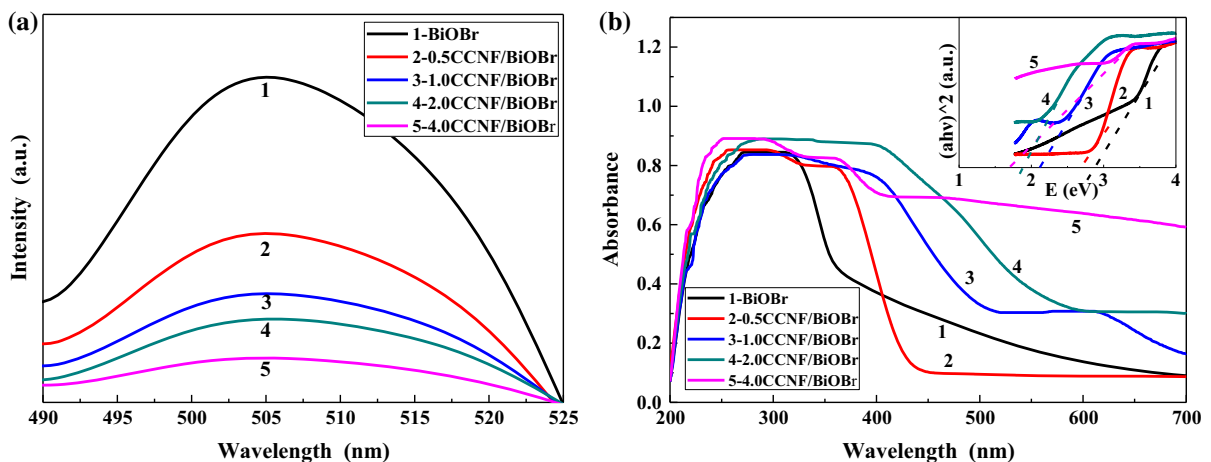

Fig. 5 a PL figure and b DRS spectra of pure BiOBr and CCNF/BiOBr composites

(4.0CCNF/BiOBr). The band gap energy (E_g) of the samples was calculated using Kubelka–Munk function, which was shown in the inset image of Fig. 5b. It could be seen that pure BiOBr had a E_g of ∼ 2.9 eV, which was close to the previous studies (Di et al. 2016), while the incorporation of the CCNF significantly narrowed the E_g of the BiOBr, in which the E_g of 4.0CCNF/BiOBr could be as low as ∼ 1.8 eV (see Table S1). The overall DRS results indicated that the photocatalytic performance of the CCNF/BiOBr composites would be better than that of the pure BiOBr.

The photodegradation of RhB was then investigated in the presence of different as-prepared photocatalysts (pure BiOBr and CCNF/BiOBr composites) under the irradiation of visible light (LED lamp). Variation of the degradation ratio of RhB (C/C_0) with the use of different photocatalysts were provided in Fig. 6a, in which pseudo first order degradation kinetics was observed for all applied catalysts. In order to analyze the degradation kinetics more clearly, scatters of the $\ln(C/C_0)$ were plotted as a function of irradiation time (Fig. 6b), in which good linear relationship was obtained between $\ln(C/C_0)$ and t. By linear fitting, the pseudo first order rate constants (k_{obs}) of RhB degradation were obtained as 0.0207, 0.0235, 0.0375, 0.0461, 0.0533 min^{-1} for 2 CCNF/BiOBr, 4CCNF/BiOBr, BiOBr, 0.5CCNF/BiOBr, and 1CCNF/BiOBr, respectively. By comparing the kinetic data, it was obviously found that the RhB degradation efficiency was significantly affected by

the CCNF content in the CCNF/BiOBr composites. Compared with pure BiOBr, the degradation performance of the CCNF/BiOBr composites increased correspondingly when the CCNF content increased to 1.0 wt%, in which all the RhB could be degraded within 90 min. When further increase the CCNF content in the composites, the degradation of RhB slowed down gradually, even lower than that of the pure BiOBr. Although the increase of CCNF content could improve the photocatalytic properties of CCNF/BiOBr based on the above characterization results, but over high content of CCNF (> 1.0 wt%) would reduce the relative ratio of BiOBr and hindered light penetration due to the darker color caused by CCNF, resulting in the less contact possibility between the photons and catalyst surfaces, and a decrease in photocatalytic activities of the 2.0CCNF/BiOBr and 4.0CCNF/BiOBr composites (An et al. 2012). Based on the above experimental results, the 1.0CCNF/BiOBr was chosen to conduct the following photocatalytic experiments.

Figure 7a shows the effects of photocatalyst dosage on the degradation performance of the RhB dye (10 mg/L). As could be seen, the degradation efficiency of the prepared catalysts enhanced with the increase of the photocatalyst dosage from 20 to 60 mg. The k_{obs} of applying 30, 40, 50, 60 mg 1.0CCNF/BiOBr was calculated as 0.0743, 0.0777, 0.0823, 0.0832 min^{-1}, respectively (see Fig. S4). It was also noted that the RhB degradation efficiency increased
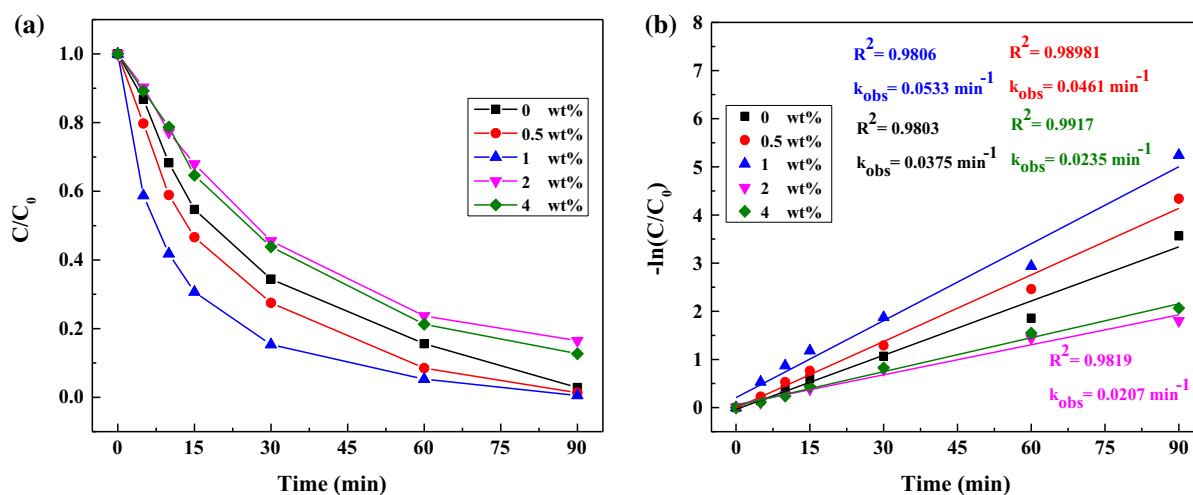

Fig. 6 Effect of CCNF contents on the **a** RhBphoto-degradation performance and **b** degration kinetics of thepure BiOBr and CCNF/BiOBr composites (RhB concentration: 10 mg/L, photocatalyste dosage: 20 mg)
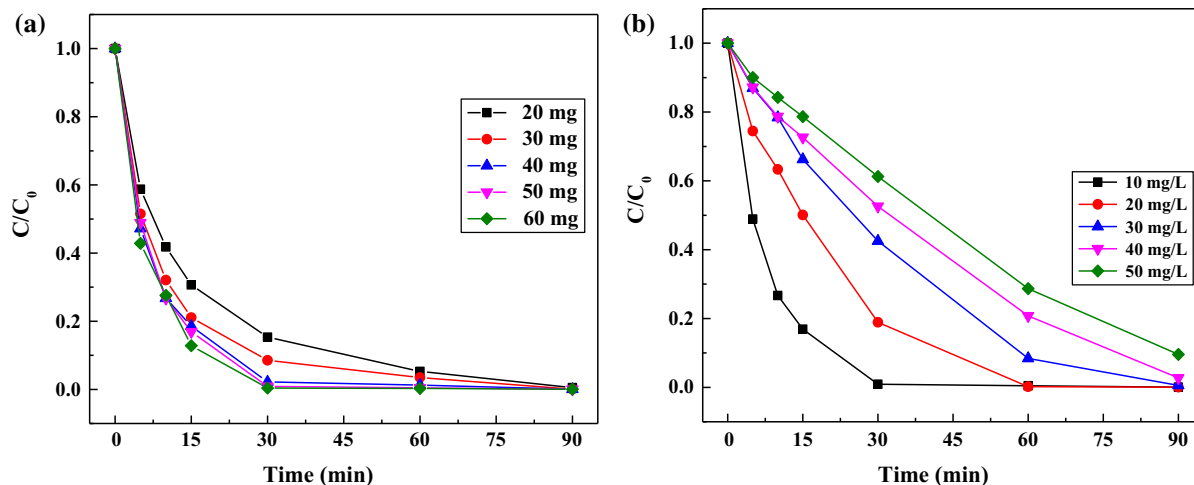
Fig. 7 Effect of **a** photocatalyst dosage and **b** dye concentration on the RhB degradation performance of the 1.0CCNF/BiOBr composites

much slower when applying higher dosage of 1.0CCNF/BiOBr (> 50 mg) compared with that of the lower dosage, which could be explained by the light shielding effect caused by the excessive catalyst particles and the aggregation of the composites in the solution system (Yuan et al. 2014).

The photocatalytic performance of the 1.0CCNF/BiOBr composite in degrading RhB with different initial concentrations varied from 10 to 50 mg/L were then studied by dosing 50 mg of the 1.0CCNF/BiOBr into the system. It could be seen from Fig. 7b that higher RhB degradation rate was obtained with lower RhB initial concentrations. Meanwhile, it could be also observed that the RhB degradation efficiency did not decreased too much when the RhB concentration increased from 10 to 20 mg/L (see Fig. S5). The main reasons which could explain this phenomenon was speculated as follows. When the RhB concentration was 10 mg/L, the relatively less RhB molecules could not occupied all the active sites on the photocatalysts surface, resulting an incomplete utilizing of the photo-generated radicals. With the increase of the RhB concentration to 20 mg/L, more active sites were occupied and more photo-generated radicals were employed to offer latter reactions, which resulted in a slower decrease of the RhB degradation efficiency. When the dye concentration continued to increase, say 30 mg/L or higher in the present study, the active sites of the photocatalysts were all occupied by the

excessive RhB molecules, leading to a lower photodegradation efficiency as a result.

In wastewater treatment process, the solution pH was considered as a significant factor influencing the efficiency of the treatment processes. Thus, the photocatalytic degradation performance of RhB by the 1.0CCNF/BiOBr was investigated at different solution pH levels (around 3, 5, 7, 9, 11), and results were given in Fig. 8. The experiments were conducted by dosing 50 mg of 1.0CCNF/BiOBr into 100 mL of 20 mg/L RhB dye solution. The obtained results showed that the solution pH significantly influenced the photodegradation efficiency of the RhB by the
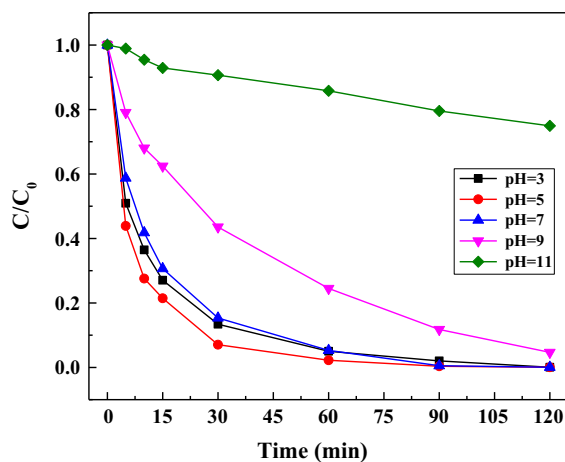

Fig. 8 Effect of solution pH on the degradation efficiency of RhB by 1.0CCNF/BiOBr composite

1.0CCNF/BiOBr composite. The photodegradation speed increased initially with the increase of the pH value from 3 to 7. The highest degradation efficiency was achieved when the pH value was 5, and almost all the RhB molecules could be photodegraded within 90 min by the 1.0CCNF/BiOBr composite, which meant the weak acid condition was beneficial to the RhB degradation effieciency. This could be explained that moderate amount of H^+ on the photocatalyst surface could attract more hydroxyl ions (OH^-) groups, which benefited the formation of hydroxyl radical ($\cdot OH$) and hence improved the degradation efficiency (Wang et al. 2015). And since the RhB was a weak basic dye, it was inclined to degrade in the faintly acidic solution. However, the photodegradation efficiency decreased when further decreased the solution pH value (< 5). This indicated that excessive H^+ hindered the contact between the OH^- and the CCNF/BiOBr surface, reducing the formation speed of the $\cdot OH$, which was harmful to the photodegradation efficiency of the RhB.

Meanwhile, the RhB degradation efficiency decreased obviously when the pH value was higher than 9. Especially when the pH value was 11, less than 25% of the RhB dye could be degraded within 120 min. When the pH value was high, the excessive OH^- could also occupy the active sites on the photocatalyst surface and hindered the contacting between the RhB molecules and the photocatalyst, reducing the photocatalytic performance as a result (Ai and Jiang 2012). The obtained results indicated that the prepared photocatalyst was applicable in a wide range of pH values from 3 to 9.

Based on the above results, the photocatalytic mechanism of the CCNF/BiOBr photocatalysts under visible light irradiation was proposed as shown in Fig. 9. When the photocatalyst was continuously irradiated by the visible light, the electron–hole pairs were activated, and the separated electrons were transited to CB from VB. Then the photo-generated electrons were rapidly transferred to the CCNF attached on BiOBr particles. Afterwards, the photo-generated electrons reacted with the oxygen molecules (O_2) to generate superoxide radicals ($\cdot O_2^-$). At the same time, the holes remained in the VB directly take part in the photo-oxidation reaction with water molecules (H_2O) to produce hydroxyl radicals ($\cdot OH$). The O_2 taking part in the photoreaction was mainly from three sources, including (1) the structural

defects of the CCNF/BiOBr composites, (2) the surface of the reaction system in contact with air, and (3) the dissolved O_2 in the solution. In the course of the photodegradation, the CCNF played an important role in improving the photocatalytic capability of the photocatalyst. First of all, the band gap of the photocatalysts was narrowed, leading to less band gap energy required for delocalizing the photo-excited electrons from CB to VB. Secondly, the CCNF possessed graphitized structure within its skeleton by high temperature pyrolysis treatment, which endowed it with excellent electronic transmission capability (Xu et al. 2015). Thus the delocalized electrons in the CB could be promptly captured by the CCNF, which hindered the quick electron–hole recombination, and provided the holes in the CB a higher probability to react with the H_2O to produce $\cdot OH$. Thirdly, since the CCNF had large specific surface area and darker color, it could provide more active sites and absorb more irradiation energy for the photocatalytic reaction, thereby increasing the photocatalytic efficiency (Luo et al. 2017). According to the above-mentioned processes, $\cdot OH$ and $\cdot O_2^-$ generated in the process were the primary oxidative species in the photodegradation RhB reactions. Therefore, the RhB dye photocatalytic efficiency could be significantly enhanced, which was ascribed to introduction of the CCNF into the photocatalyst composites.

Conclusions

In the present study, novel photocatalysts based on cellulosed derived CCNF/BiOBr composites were prepared through the combination of electrospinning, pyrolysis and hydrothermal approaches. The structural properties of the prepared composites were characterized, and the photocatalytic properties of the composites were investigated through degrading RhB dye. The results showed that through a pyrolysis treatment, the cellulose nanofibers could be transferred to carbon nanofibers with graphitic structure within their skeleton. Due to the existence of the graphitic structure, the CCNF/BiOBr composites exhibited higher photocatalytic activity compared with pure BiOBr. The overall results indicated that cellulose derived CCNF was a potential alternative to replace the traditional carbonaceous resources, and provide new insights into

Fig. 9 Illustration of the mechanism of photo-degradation of RhB by CCNF/BiOBr composites
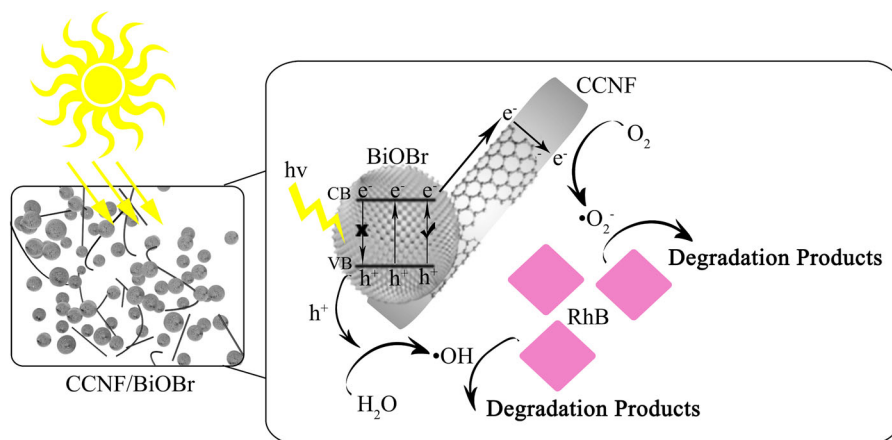
designing efficient photocatalysts from the low-cost and environment-friendly biomass materials.

References

Ai L, Jiang J (2012) Removal of methylene blue from aqueous solution with self-assembled cylindrical graphene–carbon nanotube hybrid. Chem Eng J 192:156–163. https://doi.org/10.1016/j.cej.2012.03.056

Ai Z, Ho W, Lee S, Zhang L (2009) Efficient photocatalytic removal of NO in indoor air with hierarchical bismuth oxybromide nanoplate microspheres under visible light. Environ Sci Technol 43:4143–4150. https://doi.org/10.1021/es9004366

An X, Yu JC, Wang Y, Hu Y, Yu X, Zhang G (2012) WO3 nanorods/graphene nanocomposites for high-efficiency visible-light-driven photocatalysis and NO2 gas sensing. J Mater Chem 22:8525–8531. https://doi.org/10.1039/C2JM16709C

Ao Y, Tang H, Wang P, Wang C, Hou J, Qian J (2014) Synthesis, characterization and photocatalytic activity of BiOBr–AC composite photocatalyst. Compos Part B Eng 59:96–100. https://doi.org/10.1016/j.compositesb.2013.10.045

Azzaoui K et al (2014) Synthesis and characterization of composite based on cellulose acetate and hydroxyapatite application to the absorption of harmful substances. Carbohydr Polym 111:41–46. https://doi.org/10.1016/j.carbpol.2014.04.058

Cai J et al (2016) High-performance supercapacitor electrode from cellulose-derived, inter-bonded carbon nanofibers. J Power Sources 324:302–308. https://doi.org/10.1016/j.jpowsour.2016.05.070

Carpenter AW, de Lannoy C-F, Wiesner MR (2015) Cellulose nanomaterials in water treatment technologies. Environ Sci Technol 49:5277–5287. https://doi.org/10.1021/es506351r

Chen M, Yao J, Huang Y, Gong H, Chu W (2018) Enhanced photocatalytic degradation of ciprofloxacin over Bi2O3/(BiO)2CO3 heterojunctions: efficiency, kinetics, pathways, mechanisms and toxicity evaluation. Chem Eng J 334:453–461. https://doi.org/10.1016/j.cej.2017.10.064

Choi YI, Kim YI, Cho DW, Kang JS, Leung KT, Sohn Y (2015) Recyclable magnetic CoFe2O4/BiOX (X = Cl, Br and I) microflowers for photocatalytic treatment of water contaminated with methyl orange, rhodamine B, methylene blue, and a mixed dye. RSC Adv 5:79624–79634. https://doi.org/10.1039/C5RA17616F

de Moraes ACM et al (2015) Fabrication of transparent and ultraviolet shielding composite films based on graphene oxide and cellulose acetate. Carbohydr Polym 123:217–227. https://doi.org/10.1016/j.carbpol.2015.01.034

Di J et al (2016) Advanced photocatalytic performance of graphene-like BN modified BiOBr flower-like materials for the removal of pollutants and mechanism insight. Appl Catal B-Environ 183:254–262. https://doi.org/10.1016/j.apcatb.2015.10.036

Gan L, Shang SM, Yuen CWM, Jiang SX (2015) Covalently functionalized graphene with D-glucose and its reinforcement to poly(vinyl alcohol) and poly(methyl methacrylate). RSC Adv 5:15954–15961. https://doi.org/10.1039/C5RA00038F

Gan L, Xu LJ, Qian K (2016a) Preparation of core-shell structured CoFe2O4 incorporated Ag3PO4 nanocomposites for photocatalytic degradation of organic dyes. Mater Des 109:354–360. https://doi.org/10.1016/j.matdes.2016.07.043

Gan L, Xu LJ, Shang SM, Zhou XY, Meng L (2016b) Visible light induced methylene blue dye degradation photo-catalyzed by WO3/graphene nanocomposites and the

mechanism. Ceram Int 42:15235–15241. https://doi.org/10.1016/j.ceramint.2016.06.160

Hu C et al (2014) Water-phase strategy for synthesis of TiO2–graphene composites with tunable structure for high performance photocatalysts. Appl Surf Sci 317:648–656. https://doi.org/10.1016/j.apsusc.2014.08.161

Huang Y et al (2017) Environment-friendly carbon quantum dots/ZnFe2O4 photocatalysts: characterization, biocompatibility, and mechanisms for NO removal. Environ Sci Technol 51:2924–2933. https://doi.org/10.1021/acs.est.6b04460

Jazaeri E, Zhang L, Wang X, Tsuzuki T (2011) Fabrication of carbon nanofiber by pyrolysis of freeze-dried cellulose nanofiber. Cellulose 18:1481–1485. https://doi.org/10.1007/s10570-011-9596-x

Jiang R, Zhu HY, Li JB, Fu FQ, Yao J, Jiang ST, Zeng GM (2016) Fabrication of novel magnetically separable BiOBr/CoFe2O4 microspheres and its application in the efficient removal of dye from aqueous phase by an environment-friendly and economical approach. Appl Surf Sci 364:604–612. https://doi.org/10.1016/j.apsusc.2015.12.200

Liu H, Hsieh YL (2002) Ultrafine fibrous cellulose membranes from electrospinning of cellulose acetate. J Polym Sci Part B: Polym Phys 40:2119–2129. https://doi.org/10.1002/polb.10261

Liu B, Lin L, Yu D, Sun J, Zhu Z, Gao P, Wang W (2018) Construction of fiber-based BiVO4/SiO2/reduced graphene oxide (RGO) with efficient visible light photocatalytic activity. Cellulose 25:1089–1101. https://doi.org/10.1007/s10570-017-1628-8

Luo Q, Yang X, Zhao X, Wang D, Yin R, Li X, An J (2017) Facile preparation of well-dispersed ZnO/cyclized polyacrylonitrile nanocomposites with highly enhanced visible-light photocatalytic activity. Appl Catal B-Environ 204:304–315. https://doi.org/10.1016/j.apcatb.2016.11.037

Pi L, Jiang R, Zhou W, Zhu H, Xiao W, Wang D, Mao X (2015) g-C3N4 modified biochar as an adsorptive and photocatalytic material for decontamination of aqueous organic pollutants. Appl Surf Sci 358:231–239. https://doi.org/10.1016/j.apsusc.2015.08.176

Ramirez S et al (2017) Thermal and magnetic properties of nanostructured densified ferrimagnetic composites with graphene–graphite fillers. Mater Des 118:75–80. https://doi.org/10.1016/j.matdes.2017.01.018

Tan L, Hu J, Ying Rena K, Zhu Y, Liu P (2017) Quick water-responsive shape memory hybrids with cellulose nanofibers. J Polym Sci Part A Polym Chem 55:767–775. https://doi.org/10.1002/pola.28429

Wang S et al (2015) Fabrication of a novel bifunctional material of BiOI/Ag3VO4 with high adsorption–photocatalysis for efficient treatment of dye wastewater. Appl Catal B-Environ 168–169:448–457. https://doi.org/10.1016/j.apcatb.2014.12.047

Wu Q, Li W, Tan J, Nan X, Liu S (2015a) Hydrothermal synthesis of magnetic mesoporous carbon microspheres from carboxymethylcellulose and nickel acetate. Appl Surf Sci 332:354–361. https://doi.org/10.1016/j.apsusc.2015.01.195

Wu Q, Li W, Tan J, Wu Y, Liu S (2015b) Hydrothermal carbonization of carboxymethylcellulose: one-pot preparation of conductive carbon microspheres and water-soluble fluorescent carbon nanodots. Chem Eng J 266:112–120. https://doi.org/10.1016/j.cej.2014.12.089

Xu L, Wang Y, Liu J, Han S, Pan Z, Gan L (2017) High-efficient visible-light photocatalyst based on graphene incorporated Ag3PO4 nanocomposite applicable for the degradation of a wide variety of dyes. J Photoch Photobio A 340:70–79. https://doi.org/10.1016/j.jphotochem.2017.02.022

Yuan L, Yu Q, Zhang Y, Xu Y-J (2014) Graphene-TiO2 nanocomposite photocatalysts for selective organic synthesis in water under simulated solar light irradiation. RSC Adv 4:15264–15270. https://doi.org/10.1039/C4RA01190B

Yuan D et al (2016) Synthesis and photocatalytic activity of g-C3N4/BiOI/BiOBr ternary composites. RSC Adv 6:41204–41213. https://doi.org/10.1039/C6RA05565F